Case History

Experiences with distributed acoustic sensing using both straight and helically wound fibers in surface-deployed cables — A case history in Groningen, The Netherlands

Musab Al Hasani[1] and Guy Drijkoningen[1]

ABSTRACT

Distributed acoustic sensing has been limited in its use for surface-seismic reflection measurements due to the fiber's decreased broadside sensitivity when the fiber is deployed horizontally. Deploying the fiber in a helically wound fashion has the promise of being more sensitive to broadside waves (e.g., P-wave reflections) and less sensitive to surface waves than a straight fiber (SF). We examine such claims and compare the responses of SFs and helically wound fibers (HWFs) with different wrapping angles, using standard and engineered fibers. These fibers have been buried in a 2 m deep trench in a farmland in the province of Groningen in The Netherlands, where we performed an active-source survey. We observe in our field data that using HWF has a destructive effect on the surface-wave amplitudes. Our data confirms the effect of the wrapping angle on the polarity of the surface-wave arrival and the dampening effect of the helical winding, behaving in quite a predictable fashion. Apart from the effect of the wrapping angle, the different design choices, e.g., cable filling and material type, do not show a significant effect on the amplitude of the signals. As for P-wave reflections, we observe that engineered SF and HWF provide reflection images comparable with those obtained from simultaneously deployed geophones at the surface despite the SF's decreased broadside sensitivity. A polarity reversal and an amplitude difference between the SF and HWFs are observed. Finally, we demonstrate that the combined use of SF and HWF proved to be useful because SF showed better sensitivity in the shallower part and HWF in the deeper part.

INTRODUCTION

Distributed acoustic sensing (DAS), sometimes called distributed vibration sensing, has been widely adopted for a diverse number of applications. For borehole monitoring, DAS provides dense spatially sampled data. An equivalent dense spatial sampling using geophones will be very costly. One can install optical fiber for the entire length of the borehole and use it for continuous monitoring of either repetitive active-source seismic measurements (i.e., time-lapse seismic) or for passive monitoring, similar to hydraulic fracturing (Bakku, 2015; Becker et al., 2017; Karrenbach et al., 2019). A major benefit of using DAS over geophones in such settings is that it is not disruptive during the production process. As for active seismic monitoring, early adoptions of the technology have been mostly in borehole seismic settings, so for vertical seismic profiling (VSP) (Mestayer et al., 2011; Barberan et al., 2012; Daley et al., 2013; Frignet and Hartog, 2014; Mateeva et al., 2014). The implementations of DAS in surface seismic monitoring have been limited mostly to the estimation of near-surface S-wave velocities from surface-wave signals with either active or passive sources. Examples of the use of DAS with passive sources using interferometric techniques for S-wave velocity inversion are shown in Dou et al. (2017), Ajo-Franklin et al. (2019), and Tribaldos et al. (2021). As for active-source implementations, examples include Cole et al. (2018) and Song et al. (2018).

For reflection seismic monitoring in surface deployment, field tests have been very limited due to the low sensitivity of the fiber to broadside waves (Kuvshinov, 2016). An indirect approach for obtaining surface recordings of seismic data with DAS was implemented by

Bakulin et al. (2017); their approach involved obtaining reflection data by using multiple shallow upholes. A more direct way to obtain reflection data is to install helically wound fibers (HWFs) near the surface and in a horizontal borehole (Hornman, 2017; Urosevic et al., 2018; Spikes et al., 2019). A more recent approach to enhance the broadside sensitivity is discussed in the work of White et al. (2022), for which multiple fiber configurations and arrangements are used. For multicomponent DAS measurements, theoretical models are proposed for the use of multihelix configurations to retrieve the strain-tensor components (Innanen, 2017; Ning and Sava, 2018).

In this paper, we discuss a field experiment in which we examine the combined use of straight fiber (SF) and HWF for land seismic measurements. Our focus is on the analysis of multimode information obtained from the combined use of SF and HWFs as well as assessing the usefulness of their combined use for reflection seismic monitoring.

The paper is structured as follows. In the "Introduction," we will describe the principles of DAS, how it relates to geophone data, and how it can be modeled. This is followed by describing the field experiment with the set-up and fiber configurations. The obtained results are shown and compared with each other, compared with geophone data, and our interpretations are supported by modeling. Some open points are then discussed and finally the conclusions are given.

DAS: What does it measure?

A DAS system consists of an interrogation unit, also called an interrogator, and an optical fiber, one of its ends being connected to the interrogator. It is based on the principle of optical time domain reflectometry (OTDR) for which the sensing fiber is injected with a light pulse/signal. Because the light propagates and is guided through the fiber, it encounters randomly distributed inhomogeneities infused in the fiber material, and it is scattered via the Rayleigh-scattering mechanism, which is an elastic scattering process meaning that the frequency of the incident light and the scattered light is the same. Only back-scattered light is then captured by a photodetector in the interrogator, and the phase information of the light is obtained (see Figure 1).

That relative change of distance, i.e., $\varepsilon_{xx} = (x + \delta x)/x$ due to the elastic deformation of the fiber, is proportional to the phase difference $\Delta\Phi$ of the back-scattered signal with the following relationship (Lindsey et al., 2020):

$$\Delta\Phi(t, x_i) = \frac{4\pi n L_g \xi}{\lambda}\left(\frac{x + \delta x}{x}\right), \quad (1)$$

where n is the refractive index of the fiber material, L_g is the length over which the strain is determined, the so-called gauge length, ξ is a scalar factor accommodating the changes in the index of refraction due to stress, and λ is the wavelength of the source. Here, ξ values vary between 0.79 for pure silica (Schroeder, 1980) and 0.735 for GeO_2-doped fibers (Bertholds and Dandliker, 1988). A typical value for n is 1.45 for a wavelength λ of 1550 nm (Lindsey et al., 2020).

Most DAS systems extract the temporal change of the phase, i.e., $\partial_t(\Delta\Phi)$, and therefore the output of the DAS system will be the strain rate instead of strain where $\partial_t(\varepsilon_{xx}) \propto \partial_t(\Delta\Phi)$. Several methods are used to retrieve $\Delta\Phi$, or its time-derivative; these include interferometric approaches using a single pulse (Posey et al., 2000; Farhadiroushan, 2010; Masoudi and Newson, 2017), a dual-pulse approach (Dakin and Lamb, 1990), and heterodyne approach (Hartog and Kader, 2012). More recent advances in DAS include the use of a chirp pulse as a source to allow long-range measurements of up to 171 km (Waagaard et al., 2021).

Gauge length, noise floor, and pulse repetition frequency

Several factors should be taken into consideration to measure the desirable seismic response. Here, we consider the most relevant factors that affect the DAS measurement. The first and most important one is the gauge length L_g. Here, L_g is the length over which the strain ε_{xx} is calculated, as shown in equation 1. Therefore, ε_{xx} is an average strain along L_g. Two factors determine a suitable gauge length (Dean et al., 2017), namely sampling the seismic wavefield densely and having a sufficient signal-to-noise ratio (S/N). For DAS measurement, there is a trade-off between choosing a small gauge length to sample the wavefield densely and decreasing the S/N. The choice is therefore a compromise. Another factor affecting the quality of the DAS measurement is the pulse repetition frequency (PRF) of the light source. To minimize the noise/error coming from the phase-unwrapping process, hence decreasing the noise floor, the PRF should be as high as possible but up to a certain maximum PRF_{max} to avoid overlapping with subsequent pulses (Fernández-Ruiz et al., 2019). The limit PRF_{max} can be expressed as

$$PRF_{max} = \frac{c}{2 n_g L}, \quad (2)$$

where c is the speed of light in vacuum, n_g is the group refractive index, and L is the total length of the fiber in meters. The amount of self-noise in the system coming from the system components is another factor affecting the S/N.

Sensitivity of SFs and HWFs

An intrinsic issue with DAS is that it is based on the elongation and contraction in the direction of the optical fiber. When a strain is applied at an angle θ to that fiber, a strain sensor shows a $\cos^2\theta$-amplitude dependency, as shown by Benioff (1935). Therefore, also in response to a P wave propagating with angle θ to the fiber, such a dependency is present. This means that
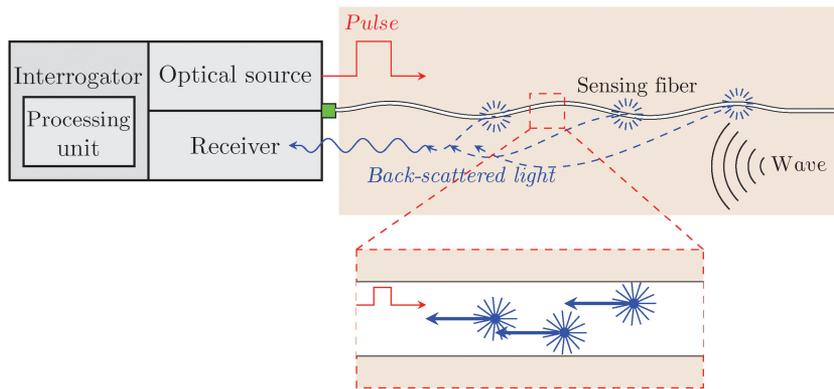

Figure 1. Illustration of DAS principle containing main components of a DAS system: an optical source sending a pulse into the fiber and back-scattered light to be captured and processed.

there is a decreased sensitivity to broadside waves. This is especially relevant in the context of surface seismic monitoring if the aim is to measure reflections; this decreased sensitivity may make it difficult to record them on horizontally surface-deployed fiber-optic cables. This is unlike DAS in borehole applications similar to VSP, for which the reflected upgoing P wavefield will have a propagation angle almost parallel to the fiber's axis (i.e., $\theta \rightarrow 0$).

To enhance the broadside sensitivity for surface-deployed cables, fiber shaping to a helix was introduced (Den Boer et al., 2012; Kuvshinov, 2016; Hornman, 2017), commonly known as HWF. An illustration of the HWF is shown in Figure 2 with two wrapping angles α of 60° and 30°, which are used in this study. Theoretically, Kuvshinov (2016) shows how the wrapping angle α affects the response to P waves, S waves, and surface waves. One outcome was that shaping the fiber into a helix will decrease its sensitivity to surface waves and enhance the fiber's sensitivity to broadside P-wave reflections.

Modeling HWF

To model the HWF response, we first start by explaining how DAS measurements are related to geophone responses (i.e., particle-velocity measurements). The DAS measurements can be equivalently represented as an estimate of the strain rate, i.e., $\dot{\varepsilon}_{xx} = \partial_t(\partial_x u_x)$, where u_x is the displacement, or as the spatial derivative in x of the x-component of the particle velocity, i.e., $\partial_x(\partial_t u_x) = \partial_x V_x$. We use the latter representation for our modeling. A 2D elastic finite-difference modeling program (Thorbecke and Draganov, 2011) will be used to estimate the velocity components and their spatial derivatives.

In the modeling, only the wrapping angle effect of the fiber is taken into account, and the mechanical properties of the fiber and the embedding cables are not included, thereby assuming the fiber and the embedding cable have the same properties as the surrounding soils/rocks. To calculate the response of HWF, we adapted the approach from Baird (2020) but used the spatial derivative of the velocity as the strain rate. Therefore, for a single helix with a wrapping angle of α, the measured response will be

$$\dot{\varepsilon}_{HWF} = \partial_x V_x \sin^2 \alpha + 0.5 \partial_y V_y \cos^2 \alpha$$
$$+ 0.5 \partial_z V_z \cos^2 \alpha. \qquad (3)$$

Because we are using a 2D elastic finite-difference scheme, expression 3 is adapted to be

$$\dot{\varepsilon}_{HWF} = \partial_x V_x \sin^2 \alpha + \partial_z V_z \cos^2 \alpha. \qquad (4)$$

We can see from this equation that for an SF $\alpha = 90°$ and the measured strain will become the one of an SF, i.e., $\dot{\varepsilon}_{SF} = \partial_x V_x$. We can combine the measurements of SF and HWF as

$$\begin{pmatrix} \dot{\varepsilon}_{SF} \\ \dot{\varepsilon}_{HWF} \end{pmatrix} = \begin{pmatrix} 1 & 0 \\ \sin^2 \alpha & \cos^2 \alpha \end{pmatrix} \begin{pmatrix} \dot{\varepsilon}_{xx} \\ \dot{\varepsilon}_{zz} \end{pmatrix}. \qquad (5)$$

In this study, we will be using this approach to compute the responses.

FIELD SET-UP

A field experiment was planned and carried out with the aim to see whether reflections could be recorded on surface-deployed fiber-optic cables and to see whether a combination of HWF and SF measurements would provide extra information, such as type of motion and type of waves. The field experiment took place on farmland in the province of Groningen, in the north of The Netherlands. A schematic representation showing the shooting line, geophone line, and buried fiber cables is shown in Figure 3a. The different optical fibers are connected via fusion splicing into two long fibers, as will be described subsequently. The interrogators were located in the farmer's shed and connected to the buried cables via a standard sin-
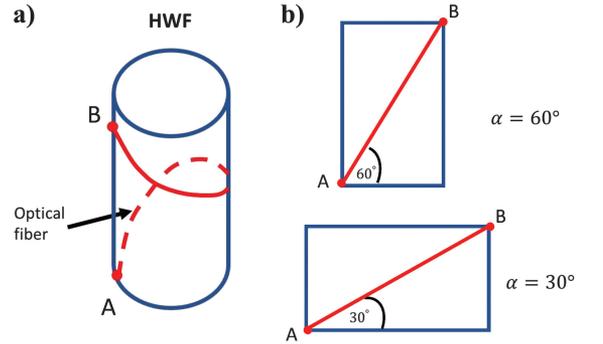

Figure 2. Illustration of the HWF: (a) a helical fiber wrapped between points A and B, (b) unwrapped fiber with two wrapping angles (i.e., $\alpha = 60°$ and $\alpha = 30°$). Adapted from Kuvshinov (2016).
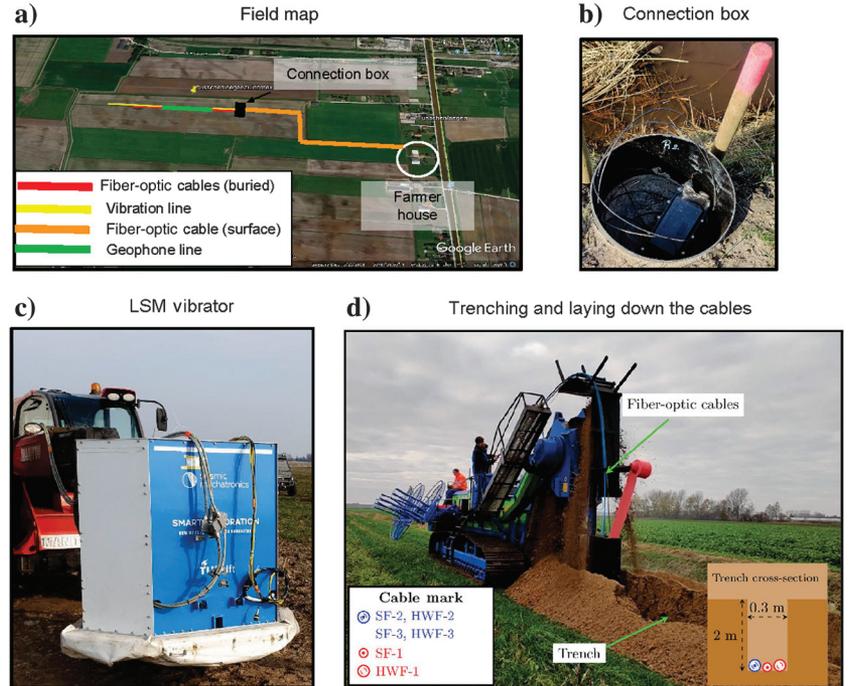

Figure 3. Field experiment set-up and components: (a) field map with the position of fiber cables (surface and buried), geophone line and vibration line, i.e., shot positions (survey location: 53°9′16.12″N, 6°50′53.99″E), (b) connection box with terminations and splices of cables, (c) electrically driven seismic vibrator, based on linear motor technology, and (d) trenching and burying fiber-optic cables.

gle-mode (SM) fiber surface cable of 1 km. Figure 3b shows the fiber's connection box that is used to check and resolve issues related to connections of the fibers (e.g., bad splices) and tap testing.

The topsoil is mostly composed of clays, peat, and some thin sand layers. A shallow borehole next to the buried cable was drilled, and P-wave and S-wave logging tools were used to measure the compressional (V_P) and shear (V_S) velocities down to around 80 m depth. These logs are shown in Figure 4. It can be observed in the figure that the near-surface down to 80 m varies for the most part around 1600–1800 m/s for V_P and 300–400 m/s for V_S except the layer between 10 m and 20 m where velocities drop to around 1500 m/s and 160 m/s for V_P and V_S, respectively. Simplified velocity models based on the logs are plotted as dashed lines in Figure 4, which will subsequently be used for modeling synthetic seismograms.

The cables are intended for continuous-passive and active time-lapse measurements and were buried 2 m deep, most of the year being below the water table. The cables were laid down by a trenching machine, commonly used for laying out drainage pipes but in this case adapted for our cables, as shown in Figure 3d. At the time of trenching, we could see that around 2 m depth the soil was quite sandy compared to the clayey/peaty topsoil, which should give us good coupling. After the cables were laid down in the trench, they were directly covered with the extracted soil by the same machine and afterward well compacted by a separate excavator.
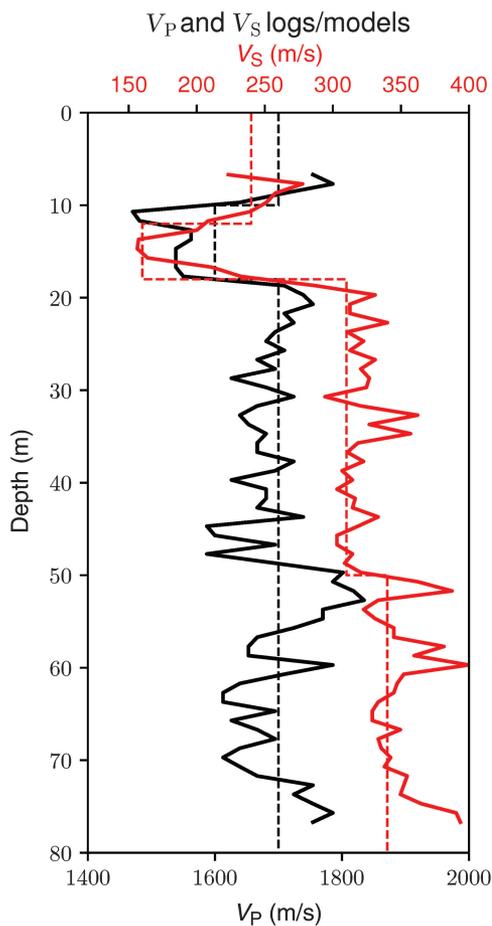

Figure 4. P-wave and S-wave velocity logs (the solid lines) of the near surface and models (the dashed lines) used for synthetics.

The source used is an electrically driven seismic vibrator, based on the technology of linear synchronous motors (Noorlandt et al., 2015); it is shown in Figure 3c. As source sweep, an upsweep of 2–180 Hz with a duration of 12 s was used, with an extra listening time of 3 s. As for source position, we shot every 2 m for a 750 m shooting line (see Figure 3a). We opted for such a dense spatial source sampling with the aim to satisfy the spatial Nyquist sampling criterion in common-receiver gathers (CRG) and to create a high-fold image. A number of two shots per position was used for vertical stacking.

Interrogator systems and fiber-optic cables

In this field experiment, we have used two DAS interrogators, namely FEBUS A1-R and iDAS™ v3. We will denote the FEBUS A1-R system as DAS standard and the iDAS v3 system as DAS-engineered for the rest of the paper. DAS standard is connected to the conventional SM fiber, and DAS engineered is connected to the engineered (i.e., Constellation™) fiber. It is important to note here that comparing the different DAS units is not the intent of this study; therefore, no direct comparison on the performance of the systems is presented. On DAS-standard, the buried cables contain the following fibers (see Figure 5a): SF-1, HWF-1 (30°), SF-2, and HWF-2 (60°). The SF-1 and HWF-1 are in separate cables, whereas SF-2 and HWF-2 are contained in the same cable. The order of fibers as shown in Figure 5a is chosen in a way to minimize optical reflections caused by splices between fibers with different core radii. As for DAS-engineered, they are connected to Constellation™ fibers SF-3 and HWF-3 (60°). Note that fibers SF-2, HWF-2, SF-3, and HWF-3 are all contained in the same cable.

DAS recording configuration

A DAS recording is a more elaborate process to configure than a geophone recording because it depends on the length of the fiber and the amount of optical loss in the fiber. Each DAS unit was configured separately to have the desired data quality. Information about the acquisition parameters used for DAS is contained in Table 1. The most important parameter to note here is the gauge length L_g, which was chosen to be 2 m for both systems. Note that even though larger gauge lengths, e.g., 10 m, are expected to give a better S/N (Dean et al., 2017), our interest was to have proper (Nyquist) sampling of the surface waves to avoid spatial aliasing of the total wavefield recordings.

Multicomponent geophones

A portion of the fiber-optic receiver line also was covered with surface-deployed 3C geophones over a length of 80 m with a spacing of 2 m. We used the horizontal in-line and the vertical components of the geophones for our comparisons because the former is linked to the strain direction of the SFs and the combination of these two components to the signal measured by HWFs. While deploying the geophones, we made sure that they were correctly oriented and properly coupled to the ground.

DATA PROCESSING

A raw measurement included the entire length of the fiber, so different fiber configurations were looped in one long stretch. The raw DAS-standard and DAS-engineered data are first down-

sampled from 10 kHz and 16 kHz, corresponding to their PRF, respectively, to a sampling frequency of 500 Hz. Then, the data are correlated with the ground force of the seismic vibrator estimated from several shots. An example of a single correlated shot record is shown in Figure 6. The beginning of the trench where the fiber gets buried is taken as position 0 m, and the fiber before that position corresponds to the surface (extension) cable. The different cables are easily identifiable on the record, as marked with the different colored rectangles below the seismograms, for which the white color rectangles correspond to extra fibers used for connecting the different fibers via fusion splicing. Figure 6 also shows the spectral content of the shot record. Via red arrows, we mark some notable noise sources showing some common-frequency modes.

Before the survey took place, the fibers were checked with an OTDR device that shows the losses and possible faults along the line. Combining these measurements with the raw data themselves, we were able to separate the different parts of the cables into different data sets with minimal uncertainty in the positions. It is difficult to exactly calibrate the distance along the fiber because the spatial resolution is limited by the spatial sampling and the gauge length of choice. With our data, the uncertainty in position is estimated at ± 1 m.

Next, processing took place for each data set and the steps are described in the following. We kept the processing quite minimal on purpose because we wanted to minimize processing artifacts. The entire processing flow is shown in Figure 7. The geometry is set, and vertical stacking is done via a diversity stack. Several noise-removal methods were applied to the data such as a trapezoid band-pass filter with corner frequencies 30/40 Hz and 100/120 Hz, *f-k* filter and bottom muting to remove the ground roll as well as some random noise. The data are then sorted into common-midpoint (CMP) gathers and corrected for normal moveout (NMO) with a constant velocity of 1700 m/s, which was determined via the vertical-component geophone data that showed clear P-wave reflections. Finally, a CMP stack is constructed using root-mean square (rms) normalization of each trace before stacking.

RESULTS

In this section, we analyze the prestack data, via common-shot gathers (CSG) and CRG, and poststack data, via CMP stacks. In the prestack domain, amplitude and polarity effects in the SFs and HWFs are studied, together with reflections observable in these prestack data. In the post-stack domain, the results of imaged reflections are discussed.

Analysis of prestack data

Horizontal component of geophone versus SF DAS

Here, we discuss the comparison in the surface-wave signal between the horizontal-component geophone (H_1) and the SF data using a CRG at 400 m and compared with synthetic shots. The
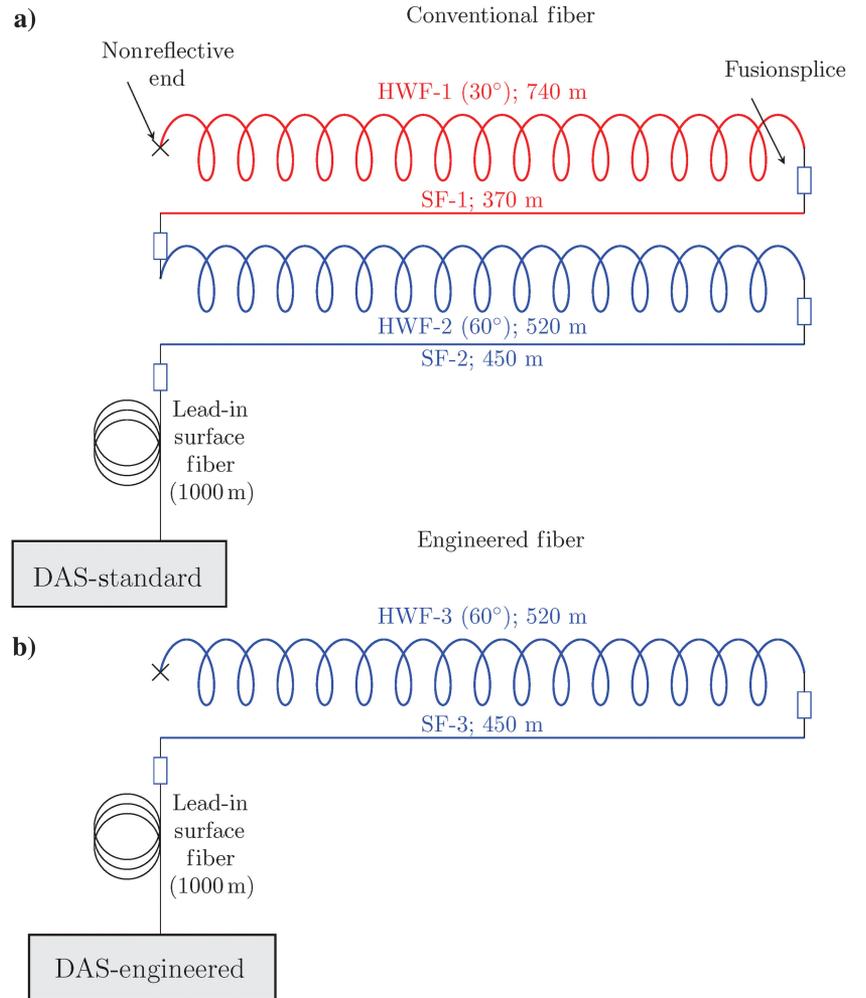

Figure 5. The DAS systems and fiber configurations: (a) DAS-standard system connected to conventional fibers and (b) DAS-engineered system connected to engineered fiber.

Table 1. The DAS systems and fiber configurations.

	DAS standard	DAS engineered
Gauge length (m)	2	2
Output spatial sampling (m)	1	1
Fiber type	Conventional single mode	Engineered single mode
Total length (m)	3300	2000
Trenched length (m)	2080	970
PRF (kHz)	10	16
Fiber segments	SF-1, HWF-1, SF-2, and HWF-2	SF-3 and HWF-3

synthetic data are modeled using a vertical-force source shot at position 400 m with a 1.5D medium based on the velocity models shown in Figure 4. The density is assumed to be constant with a value of 2000 kg/m^3. The source wavelet is a Ricker wavelet with a dominant frequency of 8 Hz. All gathers are filtered with a trapezoid band-pass filter with corner frequencies of 2/4 Hz and 8/10 Hz.

As shown in Figure 8a and 8b, we can see that the SF data are not sensitive to the direction of motion, unlike the horizontal geophones, for which the polarity is reversed going from the negative to the positive offsets. This is expected based on the synthetic examples of the modeled V_x and $\partial_x V_x$ (see Figures 8c and 8d), which agree with recorded geophone and SF data, respectively.

Response to different fiber geometry

First, we consider the amplitude differences between the different cables for one receiver position, in this case, 400 m, for all shots, as shown in Figure 9. When considering the rms values at that receiver position: even with SF-1 being in a separate (steel-armored) cable and SF-2 being part of a cable that includes SFs and HWFs, the difference in amplitude is minute. This indicates that the cable configuration and its material do not play a significant role in the case of SF. When the properties of the cable are similar to the ones of the ground around it (Kuvshinov, 2016; Baird, 2020), this can be expected, but it can here be observed that the cable design also does not affect the results. However, when we compare the amplitudes between SFs and HWFs, the difference is significant because there is an increase of 10–12 dB in favor of the SF as shown in Figure 9.

When looking at the spectra for the different fiber configurations, as shown in Figure 10, it can be observed that the main differences between SF and HWF occur in the frequency band of some 2–55 Hz, being highlighted in that figure. For data from the area under consideration, this is typically the frequency band of the surface waves and S waves. Baird (2020) notes that an HWF configuration is destructive for S waves, and therefore also for that component of the surface waves, and here this is confirmed by our observations. The helical shape acts as a (damping) filter for the surface waves and S waves. In the band above some 55 Hz, in which the information is mainly of P-wave nature (e.g., reflections and head waves), the amplitudes are comparable between the SF and HWF, suggesting that geometries preserve P-wave information, with a note that these amplitudes are *not* enhanced by the HWF configuration, although this would be expected for P-wave reflections.

Another type of observation that can be made on the CRG is the change in phase that can be observed in the surface-wave cone. Figure 11 shows the same CRG for the different fibers. We can see that the SF-1 and SF-2 give comparable results, as expected. However, a change in the polarity of the main surface-wave event around 0.4 s can be observed in the HWF-1 and HWF-2 configurations. This can be attributed to the difference in the wrapping angle. We can see that for HWF-1 ($\alpha = 30°$), the polarity is flipped when compared to the SF signal but with lower amplitude, whereas the polarity is the same for the HWF-2 ($\alpha = 60°$) as marked with the dashed red line in Figure 11b.

To explain this difference in amplitude and polarity between the SFs and HWFs, we model their response based on equation 5 with a simple model shown in Figure 4. The responses are shown in Figure 12a. Similar to what was shown in the measured data, we can see an agreement in the changes in polarity and amplitude. The polarity of SF (i.e., Figure 12b) is the same as HWF-2 ($\alpha = 60°$), and it is flipped in HWF-1 ($\alpha = 30°$) as observed in the measured data. This can be explained by equation 4 where a larger value of $\alpha = 60°$ will increase the contribution of $\partial_x V_x$ and will decrease the contribution of $\partial_z V_z$. As shown in Figure 12c, we can see that there is a difference of approximately 8–10 dB between the SFs and HWFs, which is close to the measured difference of 10–12 dB as shown in Figure 9. Therefore, we attribute the difference in amplitude to the higher sensitivity of the SF to the horizontal component and the lower sensitivity of the vertical component of the surface waves and possible S waves.

Reflections in engineered-fiber recordings

Reflections in prestack data

Here, we analyze the data collected by the DAS-engineered unit connected to the engineered fiber because those data were the best for this purpose. Figure 13a and 13b shows three CSG of each fiber type at source positions (Sx) 0 m, 10 m, and 20 m. For display purposes, the gathers are rms normalized and displayed using the same colormap range.

The first thing we can observe is that the amplitude is higher in SF-3 than in HWF-3. In Figure 13c, we look at the rms values for the time before 0.1 s (marked with the dashed red line in Figure 13a and 13b). We see that SF-3 has a higher amplitude overall, and higher amplitude variation around the mean rms value, compared
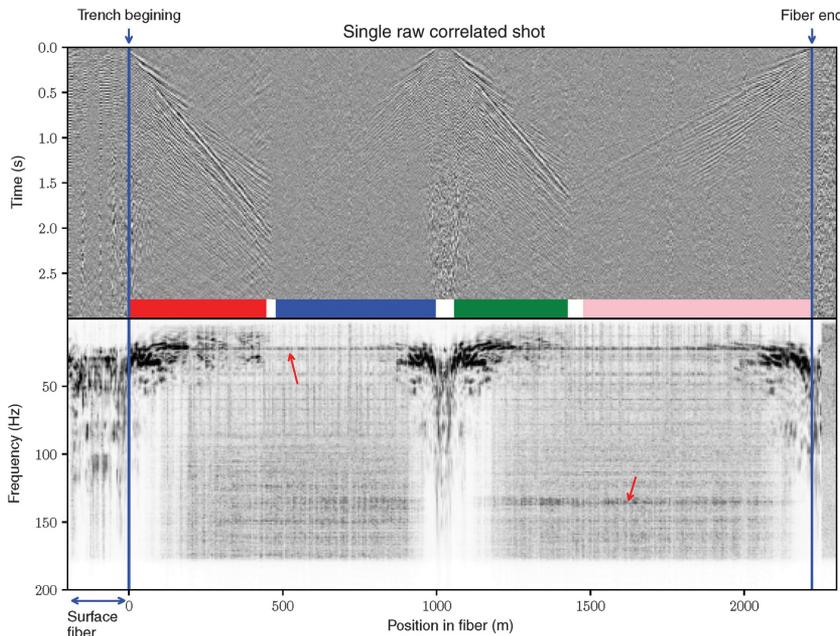

Figure 6. Correlated single raw shot of DAS-standard system in time-distance (top) and frequency-distance domain (bottom). Portions of fiber colored in red, blue, green, and pink correspond to fibers SF-2, HWF-2, SF-1, and HWF-1, respectively; white portions are splices.
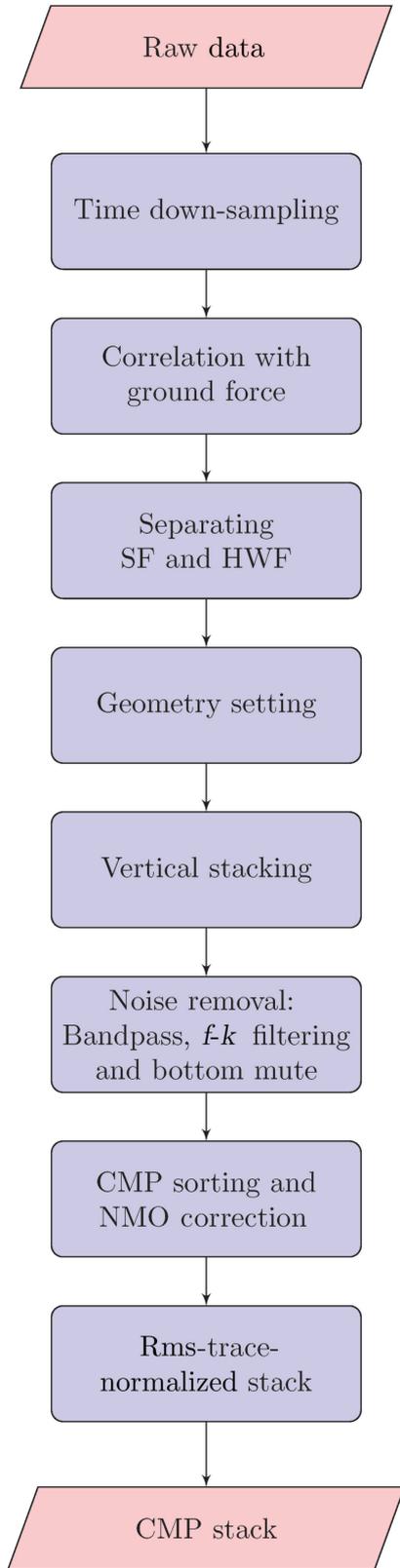
Figure 7. Processing flow to produce a CMP stack.

to HWF-3. Despite SF-3 having a higher amplitude in the early noisy arrivals, we can see the reflections (between the dashed yellow line) more clearly in the SF-3 data. Another observation in the HWF data are the horizontal events/stripes across the entire records that might be attributed to interrogator noise because the signal level [23] picked by HWF is considerably lower than SF.

Now we look at the reflections in a CRG in which the reflections seem to be more coherent. Figure 14a and 14b shows a CRG at 173 m for the SF and HWF, respectively. As for reflections, we can see three major reflection packages highlighted by the red, yellow, and green boxes. When considering the shallow reflections as highlighted by the red box, they are better discernible in the SF-3 than in the HWF-3 data. This is somewhat strange because it was expected that an SF should be less sensitive to a broadside reflection than the HWF following Kuvshinov (2016). The model described therein does not seem to match with what we observe in the field data. When following one reflection tracked by the dashed red line in Figure 14a and 14b, we can see via Figure 14c that the absolute amplitude in SF-3 is roughly twice as high as the one in HWF-3. However, we also can see that deeper events, as highlighted with the yellow box, are better discernible in HWF-3 despite the lower amplitude. Finally, the events highlighted by the green box can be seen equally well in fiber configurations, though we see some differences in the time domain and the frequency content. Due to the steeper shape of the latter moveout indicating a lower rms velocity, we interpret this event as a PS reflection. Again, also these findings do not seem to be completely in agreement with the model of Kuvshinov (2016), whereas the model showed that the [24] normalized strains should be higher in HWF for broadside reflections compared with SF for all propagation angles, but we see that we get higher amplitudes for SF in our measurements.

Modeling SF and HWF response to reflection

To model the reflections, we have adapted the near-surface velocity model in Figure 4 but added a reflector at 270 m, where the V_P
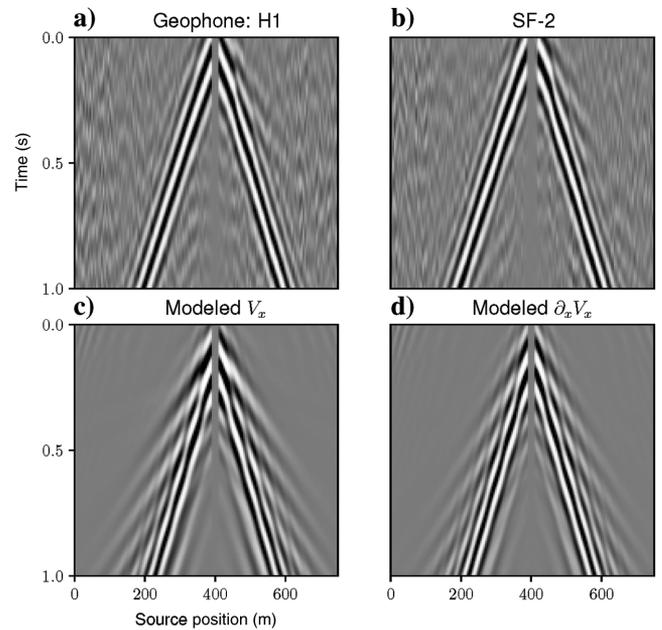

Figure 8. The CRG at 400 m: (a) recorded geophone H_1, (b) recorded SF-2, (c) modeled V_x, and (d) modeled $\partial_x V_x$.
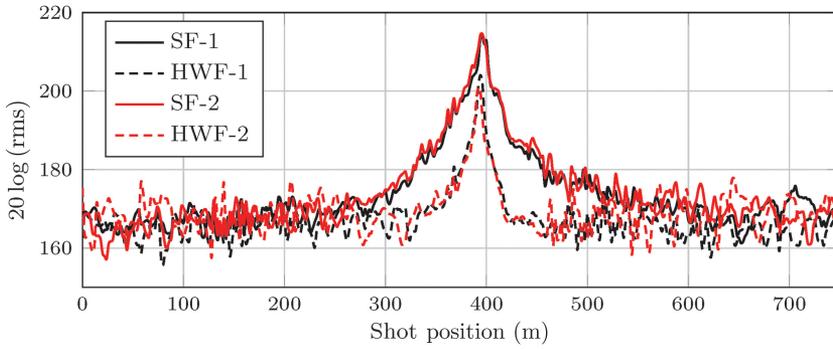
Figure 9. The rms amplitudes of CRG at 400 m of four different fiber sections connected to the DAS-standard system.
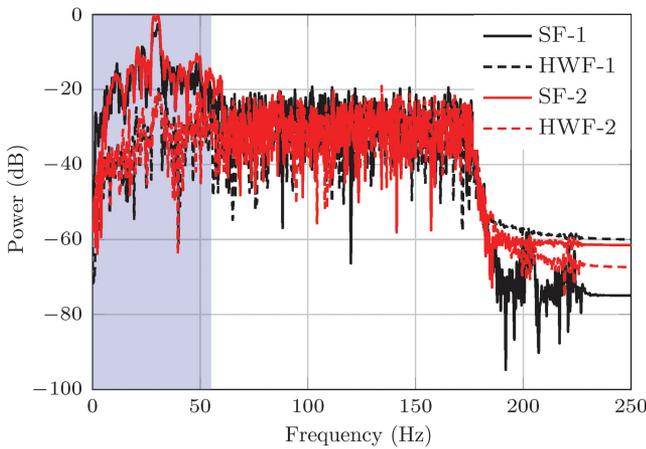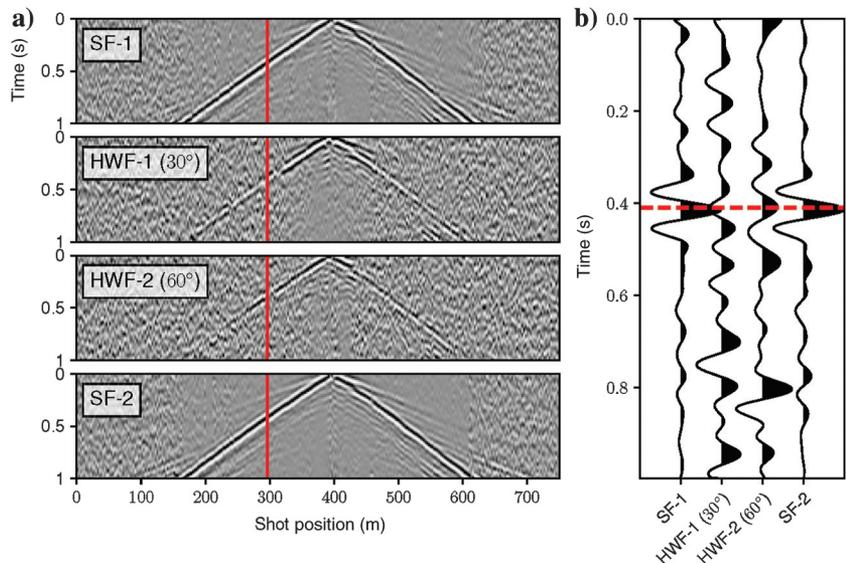

Figure 10. Power spectra of portion inside the surface-wave cone of CRG at 400 m (shot positions: 328–336 m) for different fiber configurations. Band 2–55 Hz is highlighted to indicate the main differences between HWF and SF amplitudes.

and V_S below it are 2500 m/s and 1200 m/s, respectively. The source used for modeling the synthetic data is a vertical force, and the source wavelet is a Ricker wavelet with a dominant frequency of 20 Hz. The shots for the SF and HWF are modeled using equation 5 and are shown in Figure 15a and 15b. We can see that the shot for the SF configuration shows a lower sensitivity to reflections because it mainly contains the horizontal component of the strain-rate tensor.

To analyze this further, we look at the reflections separately as shown in Figure 15a and 15b and calculate the rms amplitude for every trace at each offset, for which windows of 40 ms around the reflection are highlighted by the dashed lines in the figures. We can see that the HWF ($\alpha = 60°$) shows a higher rms amplitude for the reflection. We can see that for smaller offsets, for which the reflected wave is almost vertical, the difference in amplitude is much larger, and for longer offsets, the differences get smaller (see Figure 15c).

This modeling exercise agrees with the model discussed by Kuvshinov (2016) in terms of HWF having a higher sensitivity to broadside waves, in this case, reflections. However, it is safe to say that this model does not explain the difference in rms amplitude between SF and HWF observed for the reflections in the measured DAS data (see Figure 14).

Reflections in CMP stack

We not only analyzed CRG for the reflectivity information but also CMP stacks because they would show the quality of images that can be expected. With stacking of NMO-corrected CMP gathers, the S/N is improved substantially, especially because of the relatively high fold due to the small source and receiver spacings. Here, we present the CMP stacks derived from the SF-3 and HWF-3 data because they gave the best-quality results.

First, we consider the images produced by SF-3 and HWF-3 as shown in Figure 16 using the entire fiber length as aperture. Again, it was expected that HWF-3 would produce the highest quality

Figure 11. (a) Recorded CRG at 400 m of fibers: SF-1, HWF-1, HWF-2, and SF-2 and (b) traces at shot position 298 m (marked with the red line in [a]) showing a comparison of signals from the same offset for the different fiber configurations.

result due to the broadside sensitivity, but this was not the case. For the shallow part, as highlighted by the red box, we can even see that SF-3 provides better continuity in the main reflection marked with the red arrow. Still, deeper events, as marked with the yellow arrow, are discernible in the HWF-3 result, unlike in the SF-3 one.

Another way to compare the stacks is to look at the differences using correlation. Traces of CMP numbers 165 to 580 from each stack are windowed, tapered, and cross-correlated with each other. Then, an average cross-correlation is calculated, as shown in Figure 16c. We can see that we have a minimum around $t = 0$, indicating that the stacks are out of phase, so they have opposite polarities.

Second, we examine the continuity and presence of reflections in the SF-3 data using a comparable fold of coverage as the geophone data. Here, only a portion of the fiber is used to create the stack because the same section as the geophone line was taken for comparisons. Next to that, the DAS-receiver line was decimated spatially to the same receiver spacing as for the 3C-geophone line. As for the HWF-3 stack using the same decimated receiver line, the results did not show the reflections, unlike with what we saw with the full-fold data shown in Figure 16. This comparison between SF-3 and geophone data is shown in Figure 17.

Looking at the reference images obtained from the in-line horizontal and vertical components, V_3 gives a significantly better reflection image (see Figure 17a and 17b), as expected because most of the reflected energy is nearly vertical. The horizontal geophones

gave a worse reflection image because it is mainly sensitive to large(r) propagation angles of reflection. The V_3 image is taken as the reference image.

To compare the geophone data with our DAS measurements, we calculate the horizontal spatial derivatives of the horizontal-component geophone data (H_1) and vertical-component geophone data V_3 for every position using the expression

$$\partial_x G = \frac{\Delta G}{\Delta x_G} = \frac{G_{i+1} - G_i}{\Delta x_G}, \tag{6}$$

where G stands for geophone, the index i stands for the spatial position, and it is noted that for our case Δx_G is equal to the gauge length L_g, i.e., 2 m.

The derived strain-rate responses are shown in Figure 17c and 17d next to the SF-3 shown in Figure 17e. We can see that despite the decreased broadside sensitivity of SF-3, a reflection image can be obtained even though it is not as good as the one from the vertical geophones. For example, if we look at the reflection at 0.34 s, we can see that the reflection is flatter and more continuous in the $\partial_x V_3$ than in the SF-3. However, the same reflection is better retrieved by the SF-3 than by the horizontal in-line (H_1) geophone data in terms of its continuity. Also, shallow reflections are better shown in SF-3 data compared with the H_1 data, even though they are supposed to be mainly sensitive to the horizontal component.

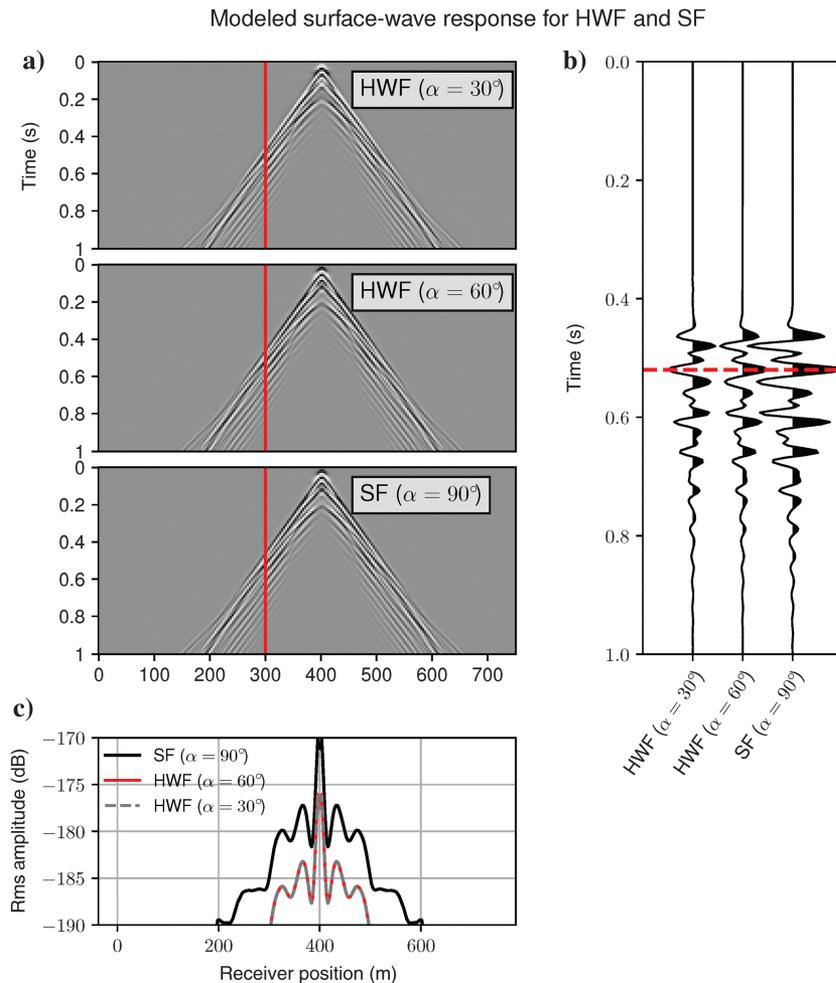Modeled surface-wave response for HWF and SF

Figure 12. (a) Modeled surface wave responses of SFs and HWFs with angles, (b) traces at receiver 300 m (highlighted by the red line in [a]) showing a comparison between the signals of fibers with different wrapping angles, and (c) rms amplitude of SF and HWF with angles.

DISCUSSION

Although, we have shown via our field data that reflections are better discernible in SF than HWF data in the shallow part, the DAS measurements are still lacking coherency compared with the geophone data. The reflectivity in this area is pretty good, also because the water table is very near the surface, which helped in detecting reflections. Good-quality systems similar to the iDAS-v3 system together with the engineered fiber are definitely needed, but systems with a better S/N would be even better.

Our data show that higher amplitudes are observed in the SF. For surface waves, this is expected and can be modeled as we have shown. However, for P-wave reflections, the models of Kuvshinov (2016) and Baird (2020) are not in agreement with our measurements, for which we saw that higher amplitudes in SF are observed in the reflection signal. We do not have a definite answer on why it is the case; however, we suspect that this might be related to the coupling of the fiber cable to the surrounding soil. The surrounding soil is very muddy and clayey with a low shear velocity of around 240–300 m/s and a P-wave velocity of around 1500–1600 m/s. Assuming this order of magnitude, our Poisson's ratio is quite high (>0.45). This is good news for SF because it transfers the strain into the horizontal fiber, but at the same time it negatively affects the HWF signal because for an impinging broadside wave, i.e., a reflection, the HWF is shortened in the vertical direction and lengthened in the horizontal direction, decreasing its overall sensitivity. Although it is not exactly the same setting, a similar observation has been recently discussed by Hendi et al. (2023), for which they modeled different scenarios of surrounding rocks and cementing conditions. They show that HWF embedded in a soft formation/cement would give a decreased strain sensitivity compared to a hard formation/cement.

Another issue is that we used HWFs, but it was already suggested by Den Boer et al. (2012) that sinusoidally shaped fibers could be used to enhance directivity in a certain broadside direction even more, but this still poses challenges (Al Hasani et al., 2020). At the time of our field experiment, we were not able to have sinusoidally shaped fibers available for the measurements.

Furthermore, our results show that the combined use of HWF and SF could provide useful insight into the wavefield components. For reflection imaging, we saw that SF-3 showed better reflection continuity than HWF-3, whereas for deeper intervals, reflections are

Figure 13. (a) The CSG at positions 0 m, 10 m, and 20 m for SF-3, (b) HWF-3, and (c) rms amplitude calculated before 0.1 s. † Cable length ≠ fiber length.
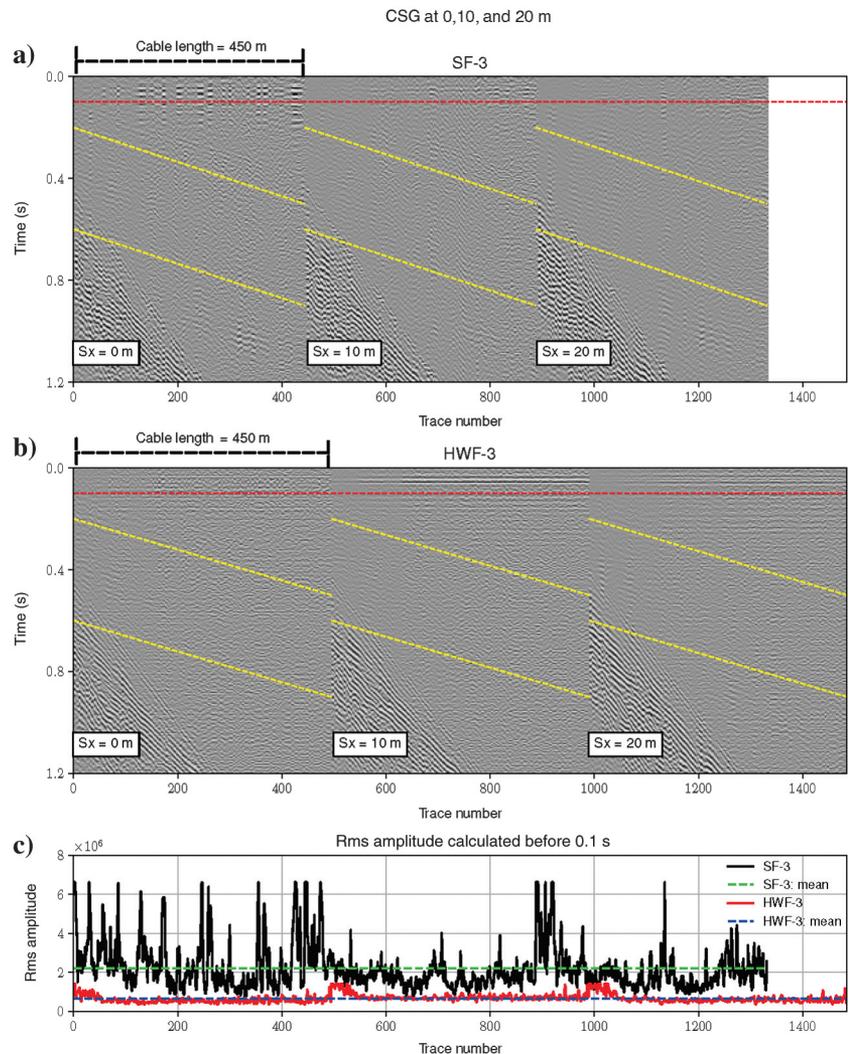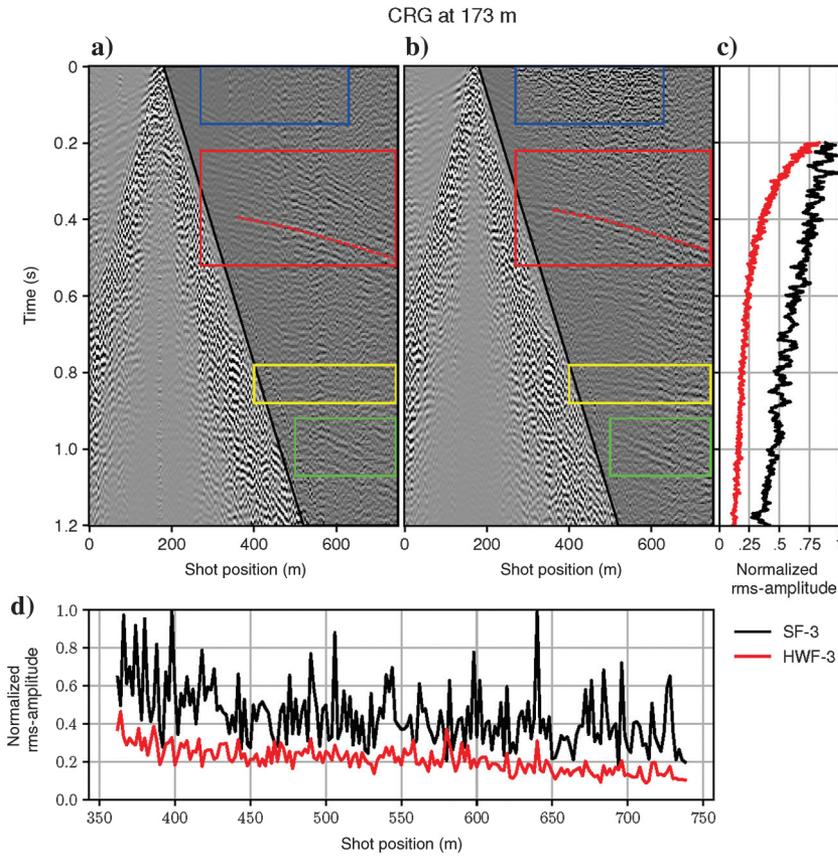
CRG at 173 m

Figure 14. The CRG at 173 m of (a) SF-3 and (b) HWF-3; (c) shows normalized rms amplitude as a function of time, calculated outside the surface-wave cone, as highlighted by the dark gray polygon and (d) rms values calculated along the reflection traced by the dashed red line within a 20 ms window. Normalized rms amplitude for SF-3 and HWF-3 calculated as: $\mathrm{rms}(\mathrm{SF}-3)/\max(\mathrm{rms}[|\mathrm{SF}-3|])$ and $\mathrm{rms}(\mathrm{HWF}-3)/\max(\mathrm{rms}[|\mathrm{SF}-3|])$, respectively.
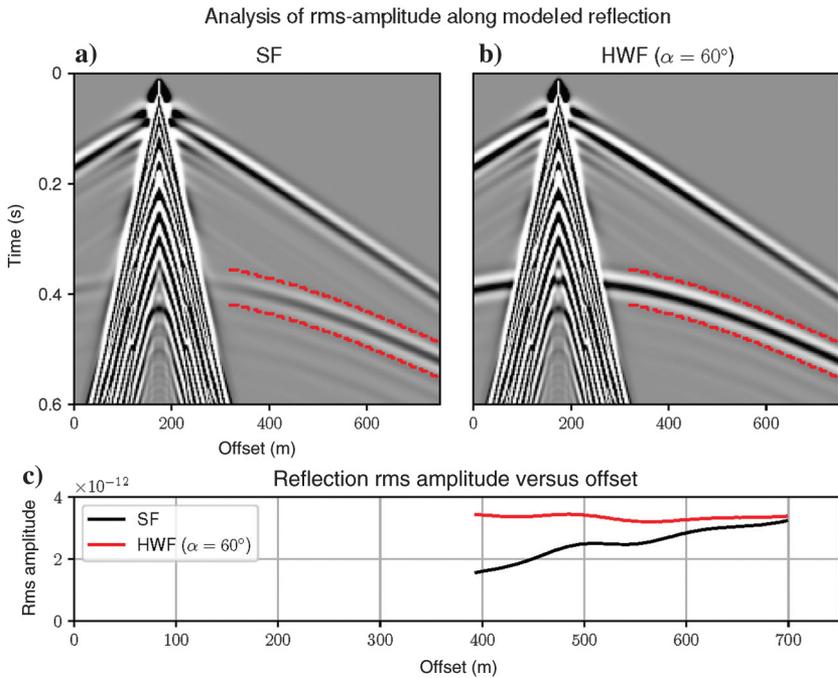
Figure 15. Modeled reflection responses and their rms amplitudes: (a) shots for SF, (b) HWF with wrapping angle of 60°, and (c) the dashed red lines highlight analysis windows of 40 ms to calculate rms amplitudes as a function of offset for the reflection.

Figure 16. The CMP-stack comparison between (a) SF-3 and (b) HWF-3, and (c) correlation function between SF-3 and HWF-3. The correlation trace in (c) is calculated from the tapered window of 0.2–0.45 s over the CMP range of 165–580.
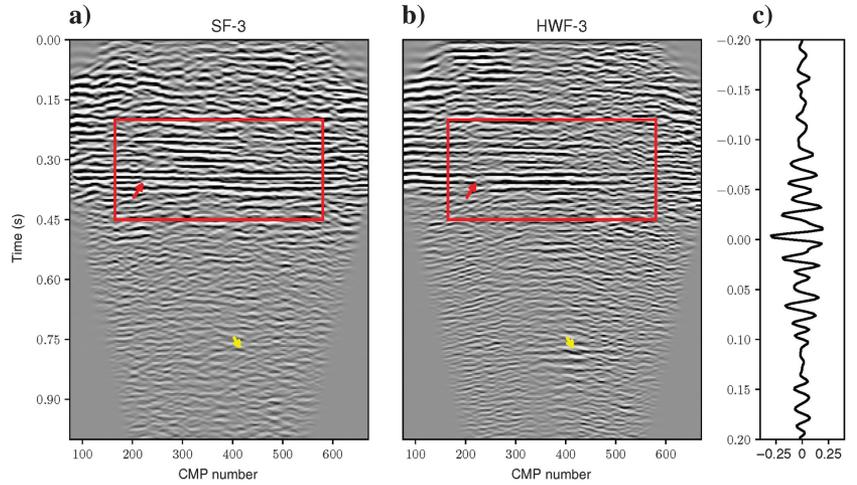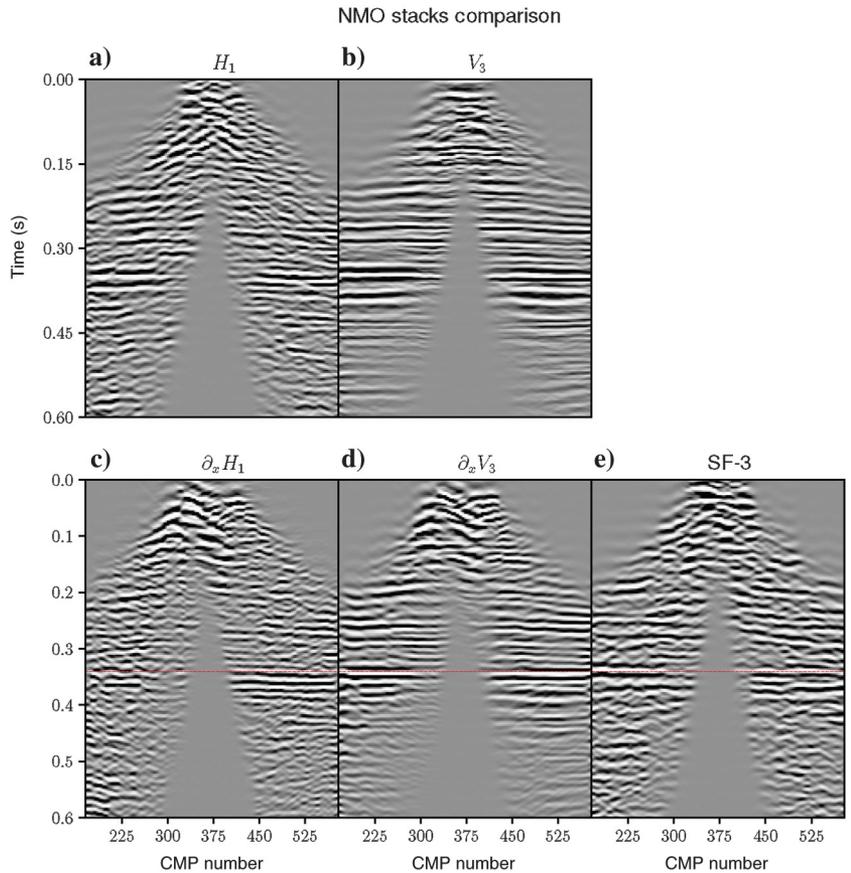

Figure 17. The CMP-stack sections for (a) geophone H_1, (b) geophone V_3, (c) (strain rate) $\partial_x H_1$, (d) (strain rate) $\partial_x V_3$, and (e) SF-3. All images are rms normalized and displayed using the same colormap limits.

(better) discernible in the HWF-3 section. This observation could be exploited in a smart combination of these two data sets.

CONCLUSION

In this paper, we examined the combined use of SFs and HWFs for land surface experiments. We conducted a field experiment in the Groningen area in The Netherlands and showed the behavior of SF and HWFs with different wrapping angles. We analyzed a typical CRG on its amplitude and some of its phase behavior. We observed higher amplitudes for surface-wave arrivals in SF data, in the typical frequency band of those waves, indicating and confirming that the HWF configuration is destructive to surface- and S-wave motion. It also was observed that the geometry of the cable design, such as cables with a separate (straight or helically wound) fiber or in an integrated fashion (with both SFs and HWFs in one cable), had little effect on the amplitude behavior. We also confirmed, via analyzing our field data and a modeling exercise, that

the wrapping angle can be such that the surface-wave arrival flips in [29] its polarity. And also, helical winding dampened that signal, as would be expected from modeling.

We saw on the field data that for reflection imaging of the engineered fiber data, the SF and the HWF data gave similar results. [30] The prestack SF data showed reflection amplitudes of some factor two higher than the ones from the HWF, something that was not expected based on the theoretical models currently in use. In the CMP-stacked data, the SF section showed more coherent and continuous reflections in the shallow part, despite its decreased broad- [31] side sensitivity, whereas for the deeper reflected events, the HWF showed slightly better results but still with lower amplitudes. It also was found that the stacked SF and HWF data showed opposite polarities for the main reflections. Still, overall, the reflection images were comparable, in terms of capturing the main reflection events but with lower quality, to the one obtained from the horizontal derivative of the vertical-component geophone data.

ACKNOWLEDGMENTS

DATA AND MATERIALS AVAILABILITY

No data have been required for this paper.

REFERENCES

Ajo-Franklin, J. B., S. Dou, N. J. Lindsey, I. Monga, C. Tracy, M. Robertson, V. R. Tribaldos, C. Ulrich, B. Freifeld, and X. Li, 2019, Distributed acoustic sensing using dark fiber for near-surface characterization and broadband seismic event detection: Scientific Reports, 9, 1328, doi: 10.1038/s41598-018-36675-8.

Al Hasani, M. A., G. Drijkoningen, and T. Reinsch, 2020, Examining directional strain sensitivity of shaped optical fibre embedded in polyurethane strip: arXiv preprint, doi: 10.48550/arXiv.2004.07277.

Baird, A., 2020, Modelling the response of helically wound DAS cables to microseismic arrivals: First EAGE Workshop on Fibre Optic Sensing, Extended Abstracts, doi: 10.3997/2214-4609.202030019.

Bakku, S. K., 2015, Fracture characterization from seismic measurements in a borehole: Ph.D. thesis, Massachusetts Institute of Technology.

Bakulin, A., P. Golikov, R. Smith, K. Erickson, I. Silvestrov, and M. Al-Ali, 2017, Smart DAS upholes for simultaneous land near-surface characterization and subsurface imaging: The Leading Edge, 36, 1001–1008, doi: 10.1190/tle36121001.1.

Barberan, C., C. Allanic, D. Avila, J. Hy-Billiot, A. Hartog, B. Frignet, and G. Lees, 2012, Multi-offset seismic acquisition using optical fiber behind tubing: 74th Annual International Conference and Exhibition, EAGE, Extended Abstracts, doi: 10.3997/2214-4609.20148798.

Becker, M. W., C. Ciervo, M. Cole, T. Coleman, and M. Mondanos, 2017, Fracture hydromechanical response measured by fiber optic distributed acoustic sensing at milliHertz frequencies: Geophysical Research Letters, 44, 7295–7302, doi: 10.1002/2017GL073931.

Benioff, H., 1935, A linear strain seismograph: Bulleting of the Seismological Society of America, 25, 283–309, doi: 10.1785/BSSA0250040283.

Bertholds, A., and R. Dandliker, 1988, Determination of the individual strain-optic coefficients in single-mode optical fibres: Journal of Lightwave Technology, 6, 17–20, doi: 10.1109/50.3956.

Cole, S., M. Karrenbach, D. Gunn, and B. Dashwood, 2018, MASW analysis of DAS fiber-optic data for active and passive seismic sources:

80th Annual International Conference and Exhibition, EAGE, Extended Abstracts, doi: 10.3997/2214-4609.201801640.

Dakin, J. P., and C. Lamb, 1990, Distributed fibre optic sensor system: WO Patent 2012030814A3.

Daley, T. M., B. M. Freifeld, J. Ajo-Franklin, S. Dou, R. Pevzner, V. Shulakova, S. Kashikar, D. E. Miller, J. Goetz, J. Henninges, and S. Lueth, 2013, Field testing of fiber-optic distributed acoustic sensing (DAS) for subsurface seismic monitoring: The Leading Edge, 32, 699–706, doi: 10.1190/tle32060699.1.

Dean, T., T. Cuny, and A. H. Hartog, 2017, The effect of gauge length on axially incident P-waves measured using fibre optic distributed vibration sensing: Geophysical Prospecting, 65, 184–193, doi: 10.1111/1365-2478.12419.

Den Boer, J. J., A. A. Mateeva, J. G. Pearce, J. J. Mestayer, W. Birch, J. L. Lopez, J. C. Hornman, and B. N. Kuvshinov, 2012, Detecting broadside acoustic signals with a fiber optical distributed acoustic sensing (DAS) [32] assembly.

Dou, S., N. Lindsey, A. M. Wagner, T. M. Daley, B. Freifeld, M. Robertson, J. Peterson, C. Ulrich, E. R. Martin, and J. B. Ajo-Franklin, 2017, Distributed acoustic sensing for seismic monitoring of the near surface: A traffic-noise interferometry case study: Scientific Reports, 7, 11620, doi: 10.1038/s41598-017-11986-4.

Farhadiroushan, M., 2010, Method and apparatus for optical sensing: WO Patent 2010136810A2.

Fernández-Ruiz, M. R., L. Costa, and H. F. Martins, 2019, Distributed acoustic sensing using chirped-pulse phase-sensitive OTDR technology: Sensors, 19, 4368, doi: 10.3390/s19204368.

Frignet, B. G., and A. H. Hartog, 2014, Optical vertical seismic profile on wireline cable: Presented at the SPWLA 55th Annual Logging Symposium, SPWLA-2014-FFFF.

Hartog, A., and K. Kader, 2012, Distributed fiber optic sensor system with improved linearity: U. S. Patent 20120067118A1.

Hendi, S., M. Gorjian, G. Bellefleur, C. D. Hawkes, and D. White, 2023, Investigation of the effects of surrounding media on the distributed acoustic sensing of a helically wound fibre-optic cable with application to the New Afton deposit, British Columbia: Solid Earth, 14, 89–99, doi: 10.5194/se-14-89-2023.

Hornman, J. C., 2017, Field trial of seismic recording using distributed acoustic sensing with broadside sensitive fibre-optic cables: Geophysical Prospecting, 65, 35–46, doi: 10.1111/1365-2478.12358.

Innanen, K. A., 2017, Determination of seismic tensor strain from HWC-DAS cable with arbitrary and nested-helix winds: 87th Annual International Meeting, SEG, Expanded Abstracts, 926–930, doi: 10.1190/segam2017-17664060.1.

Karrenbach, M., S. Cole, A. Ridge, K. Boone, D. Kahn, J. Rich, K. Silver, and D. Langton, 2019, Fiber-optic distributed acoustic sensing of microseismicity, strain and temperature during hydraulic fracturing: Geophysics, 84, no. 1, D11–D23, doi: 10.1190/geo2017-0396.1.

Kuvshinov, B. N., 2016, Interaction of helically wound fibre-optic cables with plane seismic waves: Geophysical Prospecting, 64, 671–688, doi: 10.1111/1365-2478.12303.

Lindsey, N. J., H. Rademacher, and J. B. Ajo-Franklin, 2020, On the broadband instrument response of fiber-optic DAS arrays: Journal of Geophysical Research: Solid Earth, 125, e2019JB018145, doi: 10.1029/2019JB018145.

Masoudi, A., and T. P. Newson, 2017, High spatial resolution distributed optical fiber dynamic strain sensor with enhanced frequency and strain resolution: Optics Letters, 42, 290–293, doi: 10.1364/OL.42.000290.

Mateeva, A., J. Lopez, H. Potters, J. Mestayer, B. Cox, D. Kiyashchenko, P. Wills, S. Grandi, K. Hornman, B. Kuvshinov, W. Berlang, Z. Yang, and R. Detomo, 2014, Distributed acoustic sensing for reservoir monitoring with vertical seismic profiling: Geophysical Prospecting, 62, 679–692, doi: 10.1111/1365-2478.12116.

Mestayer, J., B. Cox, P. Wills, D. Kiyashchenko, J. Lopez, M. Costello, S. Bourne, G. A. Ugueto, R. Lupton, G. Solano, D. Hill, and A. Lewis, 2011, Field trials of distributed acoustic sensing for geophysical monitoring: 81st Annual International Meeting, SEG, Expanded Abstracts, 4253–4257, doi: 10.1190/1.3628095.

Ning, I. L. C., and P. Sava, 2018, High-resolution multi-component distributed acoustic sensing: Geophysical Prospecting, 66, 1111–1122, doi: 10.1111/1365-2478.12634.

Noorlandt, R., G. Drijkoningen, J. Dams, and R. Jenneskens, 2015, A seismic vertical vibrator driven by linear synchronous motors: Geophysics, 80, no. 2, EN57–EN67, doi: 10.1190/geo2014-0295.1.

Posey, R., G. Johnson, and S. Vohra, 2000, Strain sensing based on coherent Rayleigh scattering in an optical fibre: Electronics Letters, 36, 1688, doi: 10.1049/el:20001200.

Schroeder, J., 1980, Brillouin scattering and pockels coefficients in silicate glasses: Journal of Non-Crystalline Solids, 40, 549–566, doi: 10.1016/0022-3093(80)90129-5.

Song, Z., X. Zeng, C. H. Thurber, H. F. Wang, and D. Fratta, 2018, Imaging shallow structure with active-source surface wave signal recorded by dis-

tributed acoustic sensing arrays: Earthquake Science, **31**, 208–214, doi: 10.29382/eqs-2018-0208-4.

Spikes, K. T., N. Tisato, T. E. Hess, and J. W. Holt, 2019, Comparison of geophone and surface-deployed distributed acoustic sensing seismic data: Geophysics, **84**, no. 2, A25–A29, doi: 10.1190/geo2018-0528.1.

Thorbecke, J. W., and D. Draganov, 2011, Finite-difference modeling experiments for seismic interferometry: Geophysics, **76**, no. 6, H1–H18, doi: 10.1190/geo2010-0039.1.

Tribaldos, V. R., J. B. Ajo-Franklin, S. Dou, N. J. Lindsey, C. Ulrich, M. Robertson, B. M. Freifeld, T. Daley, I. Monga, and C. Tracy, 2021, Surface wave imaging using distributed acoustic sensing deployed on dark fiber: American Geophysical Union, 197–212.

Urosevic, M., A. Bona, S. Ziramov, R. Martin, J. Dwyer, and A. Foley, 2018, Reflection seismic with DAS, why and where? 2nd Conference on Geophysics for Mineral Exploration and Mining, doi: 10.3997/2214-4609 .201802736.

Waagaard, O. H., E. Rønnekleiv, A. Haukanes, F. Stabo-Eeg, D. Thingbø, S. Forbord, S. E. Aasen, and J. K. Brenne, 2021, Real-time low noise distributed acoustic sensing in 171 km low loss fiber: OSA Continuum, **4**, 688–701, doi: 10.1364/OSAC.408761.

White, D., G. Bellefleur, K. Dodds, and Z. Movahedzadeh, 2022, Toward improved distributed acoustic sensing sensitivity for surface-based reflection seismics: Configuration tests at the Aquistore CO_2 storage site: Geophysics, **87**, no. 2, P1–P14, doi: 10.1190/geo2021-0120.1.

Biographies and photographs of the authors are not available.

Queries

1. As per SEG style guidelines, phrases such as "we propose" in the abstract should be reworded to focus on the material rather than the paper. Please check highlighted areas.

2. Rather than "so for," do you mean "such as" or "including"? Please clarify.

3. Edited as per SEG style guidelines to avoid incorrect use of "where." Please check that the original meaning of the sentence has been preserved.

4. Edited as per SEG style guidelines to avoid incorrect use of "where." Please check that the original meaning of the sentence has been preserved.

5. Edited as per SEG style guidelines to avoid incorrect use of "as." Please check that the original meaning of the sentence has been preserved.

6. Edited according to SEG style guidelines to avoid incorrect use of "where." Please check that the original meaning of the sentence has been preserved.

7. Edited according to SEG style guidelines to avoid incorrect use of "as." Please check that the original meaning of the sentence has been preserved.

8. Added as per SEG style guidelines. Please check that the original meaning of the sentence has been preserved.

9. Edited as per SEG style guidelines to avoid incorrect use of "as." Please check that the original meaning of the sentence has been preserved.

10. Edited as per SEG style guidelines to avoid incorrect use of "where." Please check that the original meaning of the sentence has been preserved.

11. Edited as per SEG style guidelines to avoid incorrect use of "as." Please check that the original meaning of the sentence has been preserved.

12. Edited as per SEG style guidelines to avoid incorrect use of "as." Please check that the original meaning of the sentence has been preserved.

13. Added as per SEG style guidelines. Please check that the original meaning of the sentence has been preserved.

14. Added for grammar accuracy. Please check that the original meaning of the sentence has been preserved.

15. Added as per SEG style guidelines. Please check that the original meaning of the sentence has been preserved.

16. Added as per SEG style guidelines to avoid incorrect use of "where." Please check that the original meaning of the sentence has been preserved.

17. Edited as per SEG style guidelines to avoid incorrect use of "as." Please check that the original meaning of the sentence has been preserved.

18. By "some" do you mean "approximately"? Please clarify.

19. Edits made for clarity. Please check that the original meaning of the sentence has been preserved.

20. By "some" do you mean "approximately"? Please clarify.

21. Edits made as per SEG style guidelines. Please check that the original meaning of the sentence has been preserved.

22. Was this intended to be a separate note on the caption? If so, this should be converted to text within the caption. Please revise.

23. Edited as per SEG style guidelines to avoid incorrect use of "as." Please check that the original meaning of the sentence has been preserved.

24. Edited as per SEG style guidelines to avoid incorrect use of "where." Please check that the original meaning of the sentence has been preserved.

25. Edited as per SEG style guidelines to avoid incorrect use of "as." Please check that the original meaning of the sentence has been preserved.

26. Missing word added. Please check that the original meaning of the sentence has been preserved.

27. Edited as per SEG style guidelines to avoid incorrect use of "as." Please check that the original meaning of the sentence has been preserved.

28. Edited as per SEG style guidelines to avoid incorrect use of "while." Please check that the original meaning of the sentence has been preserved.

29. Edited for clarity. Please check that the original meaning of the sentence has been preserved.

30. As with previous queries, please clarify your use of "some" here.

31. Edited as per SEG style guidelines to avoid incorrect use of "while." Please check that the original meaning of the sentence has been preserved.

32. Please provide complete details for the reference Den Boer et al., 2012.

Funding Information

- H2020 European Research Council (FundRef Registry ID: http://dx.doi.org/10.13039/100010663)